nature communications

Article

https://doi.org/10.1038/s41467-025-67042-7

An unconventional pathway to correlate the octahedral tilt coupling and spin-orbit reconstruction at oxide interfaces

Received: 22 January 2025

Accepted: 20 November 2025

Published online: 15 December 2025

Check for updates

Jayjit Kumar Dey[1,10,11], Koushik Jagadish[1,11], Arka Bandyopadhyay[2,11], Sourav Chowdhury[3,11], Moritz Hoesch[3], Manuel Valvidares[4], Anju Ahlawat[5,6], Feras Afaneh[7], Aryan Keshri[1], Basanta Roul[1,8], Saluru Baba Krupanidhi[1], Mukul Gupta[5], Ram Janay Choudhary[5], Thirumalai Venkatesan[9] ✉, Awadhesh Narayan[2], N. Ravishankar[1] & Sujit Das[1] ✉

The direct experimental probing and detailed imaging of octahedral tilt, along with the control of magnetic ground state and spin-orbit occupancies in an artificially engineered heterointerface through the strain manipulation via interface engineering, is the long-standing challenging issue addressed here. We introduce an innovative methodology to measure the projected O-O-O angles (O-O-O_{proj}) between the neighboring in-plane BO_6 octahedra of perovskite oxide (ABO_3), demonstrating a precise quantification of strain-manipulated octahedral tilt in atomically engineered $LaCoO_3$ (LCO)/$La_{0.7}Sr_{0.3}MnO_3$ (LSMO) bilayer interfaces. The pronounced octahedral tilt on $SrTiO_3$ (STO) substrate (tensile strain) compared to $LaAlO_3$ (LAO) substrate (compressive strain) correlates to the magnetism especially within the framework of bond angle geometry and spin-charge-orbital reconstructions, contrasting with individual single-phase films. Interfacial orbital reconstruction, Co/Mn antiferromagnetic coupling and their strain manipulation are quantified through X-ray linear dichroism (XLD) and X-ray magnetic circular dichroism (XMCD) measurements, further confirmed by both molecular orbital theory and Goodenough-Kanamori-Anderson rules. First principles calculations unveil a higher (lower) magnetic moment of individual magnetic atoms with tensile (compressive) strain, including unusual interfacial antiferromagnetism arising *d*-orbital occupations, and bond angle geometry. This endeavor paves a potential method to manipulate the octahedral tilt to tailor emergent phenomena at heterointerfaces via atomically precise strain-interface engineering.

The possibility for groundbreaking research lies at the interface of robust perovskite systems, where control of spin, charge, orbital, and lattice interactions holds immense possibilities from both fundamental and device perspectives[1–3]. To unravel the correlations among these diverse degrees of freedom, numerous approaches are being studied, including engineering of strain[4,5], interface[6,7], defects[8,9] and symmetry[10,11]. However, scant attention has been paid to engineering bonding geometry within and in-between metal–oxygen octahedra[12].

A full list of affiliations appears at the end of the paper. ✉e-mail: venky@ou.edu; sujitdas@iisc.ac.in

Particularly challenging is the precise quantification and systematic manipulation of oxygen octahedral tilting, rotation, shape alteration, as determining the positions of oxygen ions at interfaces through diffraction techniques or conventional electron microscopy, with the unit-cell-by-unit-cell observation of the oxygen network, is exceedingly complex. Several models have been proposed to generally describe how oxygen octahedral tilting evolves at perovskite oxide interfaces with different patterns[13,14] and also presented octahedral tilting in antiperovskite oxide and halide perovskite via first-principles calculations[15,16]. However, these models often overlook differences in the direction of tilting axes, magnitude of tilting angles, and orientation of the interfaces among different tilted components which offer an unconventional and efficient method for tailoring a myriad of functional properties in transition metal oxides. Manipulation of octahedral tilting is a key parameter for controlling the functional properties of oxides. In recent years, induced octahedral tilting ordering has demonstrated the potential for significant functional enhancements, such as magnetoelectric switching in multiferroics[17,18] and improved optoelectronic properties in inorganic halide perovskites[19]. Several approaches, such as epitaxial strain, thickness manipulation, Jahn-Teller distortion, and stoichiometry control/ cation off-centering, have also been suggested for tuning octahedral tilt and distortions[20–22]. Octahedral tilting can alter the point symmetry of B-site ions, thus influencing Jahn–Teller distortions linked to crystal-field splitting of *d* orbitals[23], or breaking inversion symmetry[24], which directly impact the hybridized states between oxygen *p* and neighboring A-site or B-sites orbitals, profoundly affecting the electrical, magnetic, and superconducting properties of numerous perovskite compounds[25]. However, their effectiveness is constrained by the demand for high-quality interfaces. Interestingly, the unstrained perovskite $LaCoO_3$ (LCO) is merely an insulator and non-magnetic (paramagnetic) material that exhibits a systematic temperature-dependent spin-state transition starting from a low spin state (LS, t_{2g}^6, S = 0) to an intermediate spin state (IS, $t_{2g}^5e_g^1$, S = 1) or a high spin state (HS, $t_{2g}^4e_g^2$, S = 2)[26–28]. Nevertheless, the single layer LCO thin films can exhibit unusual ferromagnetic insulator (FMI) behavior with Curie temperature (T_C) ranging from 24-92 K, depending on the substrate-induced strain[15–17]. The rare presence of FMI nature holds promise for applications in spin-filter magnetic tunneling and multiferroic-based spintronics device applications. In parallel, the interface of an insulating ferromagnetic LCO with a double-exchange half-metallic ferromagnetic manganite $La_{0.7}Sr_{0.3}MnO_3$ (LSMO) has aroused great interest due to its display of interfacial octahedral tilt, room temperature charge transfer, spin transition as well as orbital polarization[29]. Furthermore, the mixed-valency, as well as the half-filled e_g orbital of Mn^{3+} in LSMO, ensures the crucial role of its magnetic and electronic properties via lattice distortion and orbital ordering through strain engineering[30–32]. The microscopic origin of these observed effects, artful manipulation of magnetic ground states, spin-orbital reconstruction and their low temperature scenario in the presence of tensile strain and compressive strain (for instance using Aberration-Corrected Scanning Transmission Electron Microscopy (AC-STEM)), remains largely uncharted.

Furthermore, when subjected to tensile and compressive strains, the octahedral tilt (even at room temperature) provides a crucial pathway to explore multifunctional properties. This study aims to fill that gap by presenting experimental evidence of octahedral tilt and manipulation under tensile to compressive strain, showcased through AC-STEM. Herein this study, we employ an innovative methodology incorporating O-O-O angles rather than conventional B-O-B angles to precisely quantify and characterize the octahedral tilt by incorporating AC-STEM with a greater applicability across various perovskite (oxide, halide, antiperovskite) materials and exploring the impact of substrate-induced strain spanning from compressive to tensile. Our systematic study on X-ray absorption spectroscopy (XAS) confirms the charge state, showcasing the genuine presence of high spin Co^{2+} and Mn^{4+} at the bilayer interfaces. X-ray linear dichroism (XLD) analysis suggests that strain controls the in-plane and out-of-plane orbital polarization switching at the heterointerfaces. X-ray magnetic circular dichroism (XMCD) depicts element-specific insights into the manipulation of the interfacial magnetic ground state, correlating with the antiferromagnetic nature at Co/Mn interfaces and magnetometry data. Finally, first-principles calculations lend further support for the role of the octahedral tilt under strain and the reconstruction of spin-charge-orbital-lattice degrees of freedom. The obtained results highlight an attractive strategy to design, engineer, and manipulate the strain-interface controlled octahedral tilt and the resultant surface-to-interfacial tunable properties open up avenues for next-generation spintronic devices involving oxides.

Results and discussion

Structural-Interfacial resolution and octahedral tilting

5 nm LSMO/10 nm LCO bilayers (BL) films (with alternative growth sequence denoted as BL1 and BL2; where capped LSMO (top) on LCO film is denoted as BL1—LSMO/LCO, while capped LCO (top) on LSMO film denoted as BL2—LCO/LSMO), were grown on single crystalline (001)-oriented AlO_2 terminated $LaAlO_3$ (LAO), TiO_2 terminated $SrTiO_3$ (STO), and $Pb(Mg_{1/3}Nb_{2/3})O_3$-$PbTiO_3$ (PMN-PT) substrates using a reflection high energy electron diffraction (RHEED)-assisted pulsed laser deposition system (details in Methods, Supplementary note I, Supplementary Figs. 1-3). Bragg reflections reveal the single crystalline phase of LSMO and LCO in the BLs, as well as gradual shifts of (00 *l*) peaks towards lower angles from LAO to PMN-PT (Supplementary Fig. 4a-b, Supplementary Fig. 5), indicating that the BLs on LAO are under compressive strain, while the BLs on STO and PMN-PT are under tensile strain. Simultaneously, the calculated out-of-plane lattice parameter for LSMO and LCO layers undergo an evolution from 3.94 to 3.89 Å and 3.84 to 3.80 Å respectively, while transitioning from LAO to PMN-PT substrates (Supplementary Fig. 4c). The deposited BLs exhibited smooth surface, with an average root-mean-squared roughness value close to 300 pm for all the BLs as confirmed from atomic force microscopy (AFM) (Supplementary Fig. 4d). In addition, x-ray reciprocal space mapping (RSM) along (103)-reflection confirms the coherent strain of bilayers on LAO and STO i.e. the bilayers share the same in-plane lattice constant with LAO and STO (Supplementary Fig. 4e-f, Supplementary Fig. 5), while bilayer on PMN-PT showed a vertical shift due to lattice relaxation, affirming compressive strain of BLs on LAO (LSMO: −2.07%, LCO: −0.5%), the tensile strain on STO (LSMO: +0.9%, LCO: +2.4%), and higher tensile strain on PMN-PT (LSMO: +1.8%, LCO: +3.2%) (Supplementary Fig. 4g).

The high-angle annular dark-field (HAADF) micrograph exhibits an atomically sharp interface between the film layers and the substrate of the BL2 on STO (Fig. 1a; details in Methods and Supplementary Figs. 6-7), while an atomic-resolution energy dispersive X-ray spectroscopy (EDS) was utilized to precisely locate multiple interfaces due to the insufficient contrast between LSMO and LCO layers (Fig. 1b-c). A similar investigation using HAADF-STEM and atomic-resolution EDS mapping was conducted on BL2 on the LAO substrate (Fig. 1d-f), revealing the distribution of La, Sr, Al, Mn, and Co atoms at atomically smooth interfaces. Specifically, the Mn map was utilized to determine the precise number of LSMO layers, revealing that both samples consisted of 15 Mn layers. This information plays a key role in quantifying octahedral tilts across the interfaces, as discussed later. Additionally, STEM analysis of BL2 on PMN-PT substrate indicated severe distortion in LSMO planes near the LSMO/PMN-PT interface (Supplementary Fig. 8a-c). This distortion manifested as the stretching of the in-plane lattice of the LSMO layer to fit into the larger PMN-PT lattice, resulting in a local structural deformation and contrast variation. A form of edge dislocation, marked by a dashed circle (Supplementary Fig. 8d), accommodated the strain relaxation, with LSMO layers above the dislocation displaying uniform contrast and additional lattice planes

https://doi.org/10.1038/s41467-025-67042-7

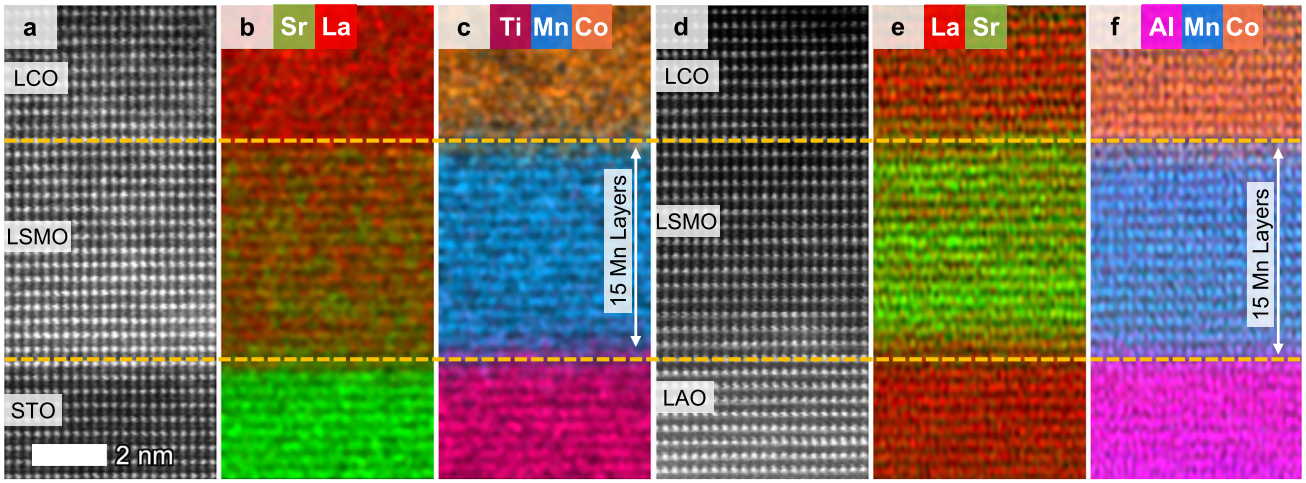

Fig. 1 | Microscopic structural characterization of the LCO/LSMO BLs under strain. a Atomically resolved STEM-HAADF micrograph of the BL2 on STO substrate. **b**, **c** EDS elemental maps from the same region as (**a**), using which the interfaces are marked and observed to be atomically sharp, with a diffuseness of the order of one unit cell. **d-f** Atomically resolved STEM-HAADF micrograph of the BL2 on LAO substrate and the corresponding EDS maps. The Mn map can be used to pinpoint the two interfaces, using which it is observed that the LSMO film consists of 15 Mn layers as shown in (**c**) and (**f**); This information can be correlated with the ABF micrograph to exactly measure the variation in the octahedral tilts across the interfaces, down to the unit cell level. The scale is the same as shown in (**a**) for all the images.

compared to those below, indicating relaxation. These findings support observations from reciprocal space mapping (RSM), confirming relaxation in BL2 on the PMN-PT substrate. The impact of strain was further investigated by growing a thicker BL2 film (consisting of ~18 nm LSMO bottom layer on a PMN-PT substrate first, followed by a 5 nm LCO top layer). The substantial strain induced by the PMN-PT substrate results in pronounced dislocations within the LSMO layer, particularly near the LSMO/PMN-PT interface. However, no dislocations are observed at the LCO/LSMO interface, suggesting that the strain effects are significantly relaxed as the film thickness increases (Supplementary Fig. 9).

The strain effects on the LCO/LSMO bilayer across various substrates were further validated through peak-pair analysis (PPA) strain mapping using high-resolution STEM micrographs (Supplementary Fig. 10a, d), with the lattice spacing of the substrate serving as a reference. The in-plane PPA strain maps (Supplementary Fig. 10b) demonstrate uniformity, indicating that the lattice parameter of the LSMO film closely matches that of the STO substrate. This suggests that the LSMO layer is coherently stretched to fit the substrate, achieving the desired strain as per the experimental design. However, out-of-plane relaxation is observed in the LCO layer of the BL2 on the STO substrate (Supplementary Fig. 10c). Similarly, in the case of BL2 on LAO substrates, no significant changes in the in-plane lattice parameter were observed relative to the substrate, as the LSMO layer is coherently compressed onto the LAO lattice (Supplementary Fig. 10e). Particularly, substantial out-of-plane relaxation of the LSMO layer is evident (Supplementary Fig. 10f). These high-resolution STEM-PPA results align with the XRD and RSM (Qz) findings, reinforcing the successful control of strain within the bilayer films and validating the strain engineering approach employed in the study.

Octahedral tilts, a dominant factor in the physical behavior of perovskite oxides, were directly confirmed and quantified using the projected O-O-O angle (O-O-O_{proj}) between two in-plane neighboring octahedra. Since the presence of geometric tilt of the octahedra will inevitably cause a systematic displacement of the O atoms, a non-coplanarity in the in-plane O column positions is expected (which appears as a non-collinearity in the [110] projection under consideration). The O-O-O_{proj} angle will be 180° for perfectly coplanar O atoms, and any deviations from this indicate that the O atoms are non-coplanar. The O-O-O_{proj} angle can thus be used as a probe to primarily assess the presence of actual geometric octahedral tilt, while effectively filtering out other contributions such as the B-ion displacement and octahedral distortions. This method is also observed to be robust against experimental errors as compared to the conventional B-O-B angles (details in Supplementary Note II). Furthermore, we have assumed that the projected B-O-B and O-O-O angles should ideally be the same, provided the B site ion is not displaced and the octahedra are stiff, as a first approximation to filter out the other components (details in the methods section and Supplementary Figs. 11-13). This is shown schematically (Fig. 2a-c) for a hypothetical perovskite with a displaced B-ion, a standard STO lattice without any distortion/tilting, and LSMO which possess actual octahedral tilt, respectively (details in Methods). Simultaneous HAADF and annular bright field (ABF) imaging of the BL on STO facilitates the direct localization of cations and oxygen atoms, which is crucial for comprehending the octahedral tilt behavior (Fig. 2d-e; details in Methods). The absence of octahedral tilt in the STO substrate region is evident, with an O-O-O_{proj} angle close to 180°, signifying coplanar oxygen atoms in any given BO plane (Fig. 2f-g). However, a drastic change occurs across the LSMO/STO interface, with the O-O-O_{proj} angle reaching ~173° up to 5 uc, indicating non-coplanar oxygen atoms due to octahedral tilt in the LSMO layer. The O-O-O_{proj} angle variation continues throughout the LSMO layer, reaching ~175° at the LCO/LSMO interface. Digitally magnified micrographs of the LCO/LSMO and LSMO/STO interfaces (Fig. 2h-i) reveal a clear signature of octahedral geometry, with observable alternating shifts of oxygen atom positions both upward and downward along the horizontal Co−O−Co and Mn−O−Mn sequences. This alternating shift suggests octahedral tilts in both CoO_6 and MnO_6 near the LCO/LSMO interface, providing valuable insights into the detailed structure of these perovskite oxide bilayers.

In contrast, HAADF-ABF imaging of LCO/LSMO BL on LAO substrate (Fig. 2j-m) revealed a consistent tilt angle of ~178° across the LSMO and LAO layers, with a slight deviation to ~173° at the LCO/LSMO interface (Fig. 2m). Unlike the pronounced octahedral tilt observed in LCO/LSMO BL on STO, a constant tilt angle was observed at the LCO/LSMO and LSMO/LAO interfaces (Fig. 2n-o). The possibility of the octahedral tilt into the plane of the figure (along an axis in the plane of the figure), was considered a possible explanation for the non-appearance of the octahedral rotation in the experimental image, which is possible due to the absence of 4-fold symmetry in LSMO and LCO layers (details in Method, Supplementary Fig. 14). Further

https://doi.org/10.1038/s41467-025-67042-7

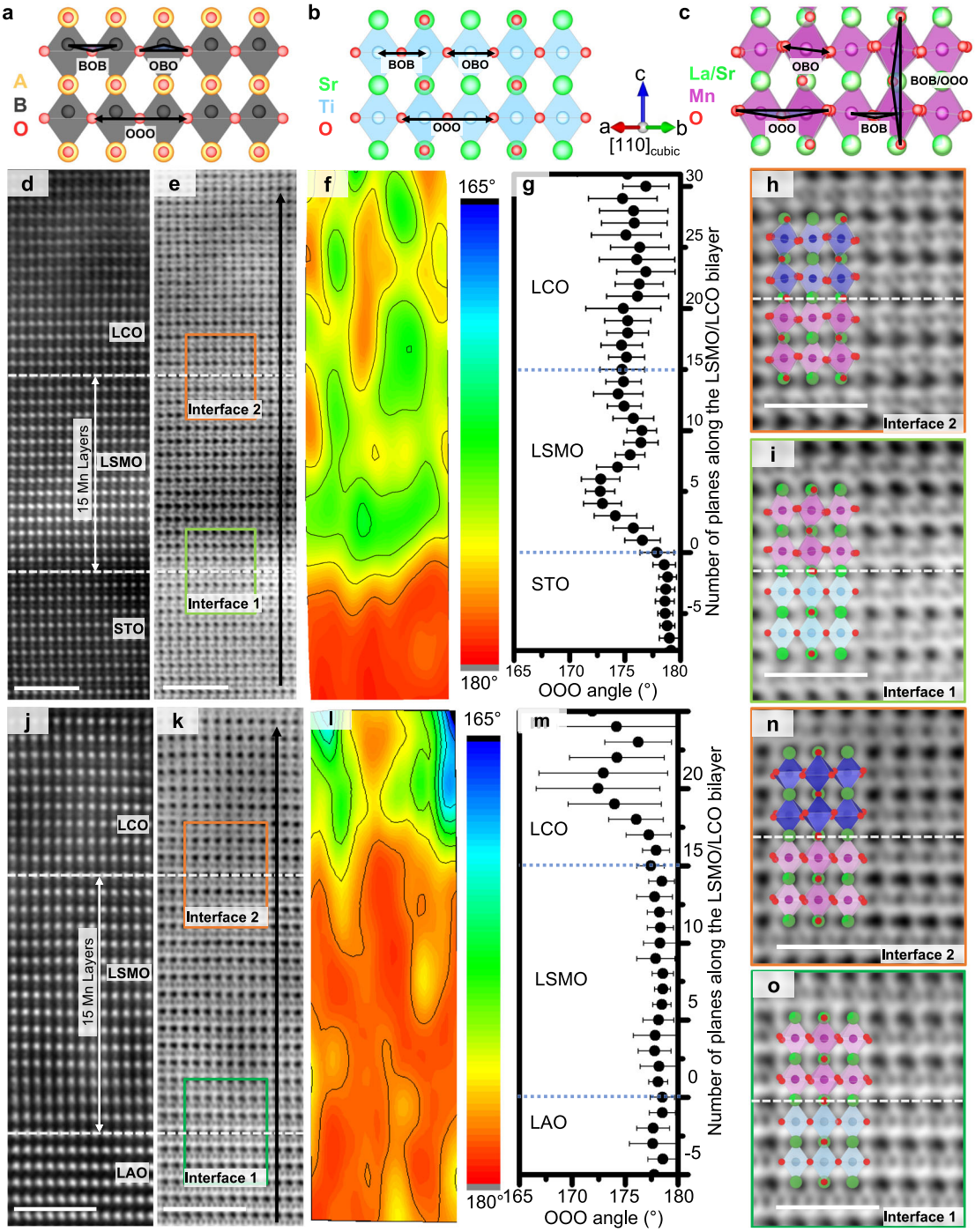

Fig. 2 | Octahedral tilt under strain of the LCO/LSMO BLs. a-c Schematic representations showing the selective detection of octahedral tilting using the O-O-O_{proj} angles, highlighting that the B-O-B_{proj} angles are less effective in distinguishing between octahedral tilting and distortion. **d**, **e** HAADF-STEM and ABF micrographs of the BL2 on STO substrate. **f**, **g** Contour mapping of the O-O-O_{proj} angles based on the oxygen atom coordinates, and the row-averaged O-O-O_{proj} angle plotted as a function of distance from the LSMO/STO interface. **h**, **i** Digitally magnified images of the two interface with the overlaid structural schematic, depicting the TiO_6, MnO_6 and CoO_6 octahedra corresponding to the STO, LSMO and LCO layers, respectively. **j**, **k** HAADF-STEM and ABF micrographs of the BL2 on LAO substrate. **l** The O-O-O_{proj} angle contours mapped to the O coordinates and, **m** The row-averaged O-O-O_{proj} angle plotted as function of the planar distance from the LSMO/LAO interface. **n**, **o** Digitally magnified images of the two interface regions with the overlaid structural schematic, directly visualizing that the O atoms are effectively coplanar along the particular projection. Scale bar in (**d, e, j, k**) represents 2 nm, and scale bar in (**h, i, n, o**) represents 1 nm. The projected TiO_6 and AlO_6 octahedra of the STO and LAO substrates are represented by the light blue octahedra, while the MnO_6 octahedra of LSMO and the CoO_6 octahedra of LCO are represented by the pink and dark blue octahedra, respectively in (**h**, **i**, **n**, **o**).

investigation using foils sectioned along a perpendicular orientation showed the same behavior, ruling out the possibility that the absence of rotation was an experimental artifact (Supplementary Figs. 6, 14-16). Furthermore, the O-O-O angles from the LAO substrate show a slight deviation from the ideal 180° (~3 degrees) in both foils. Since this deviation from 180° is observed in two different foils from the LAO substrate (Fig. 2m and Supplementary Fig. 16d), while being much less in the STO substrate (Fig. 2g), suggests that this feature is not due to

https://doi.org/10.1038/s41467-025-67042-7

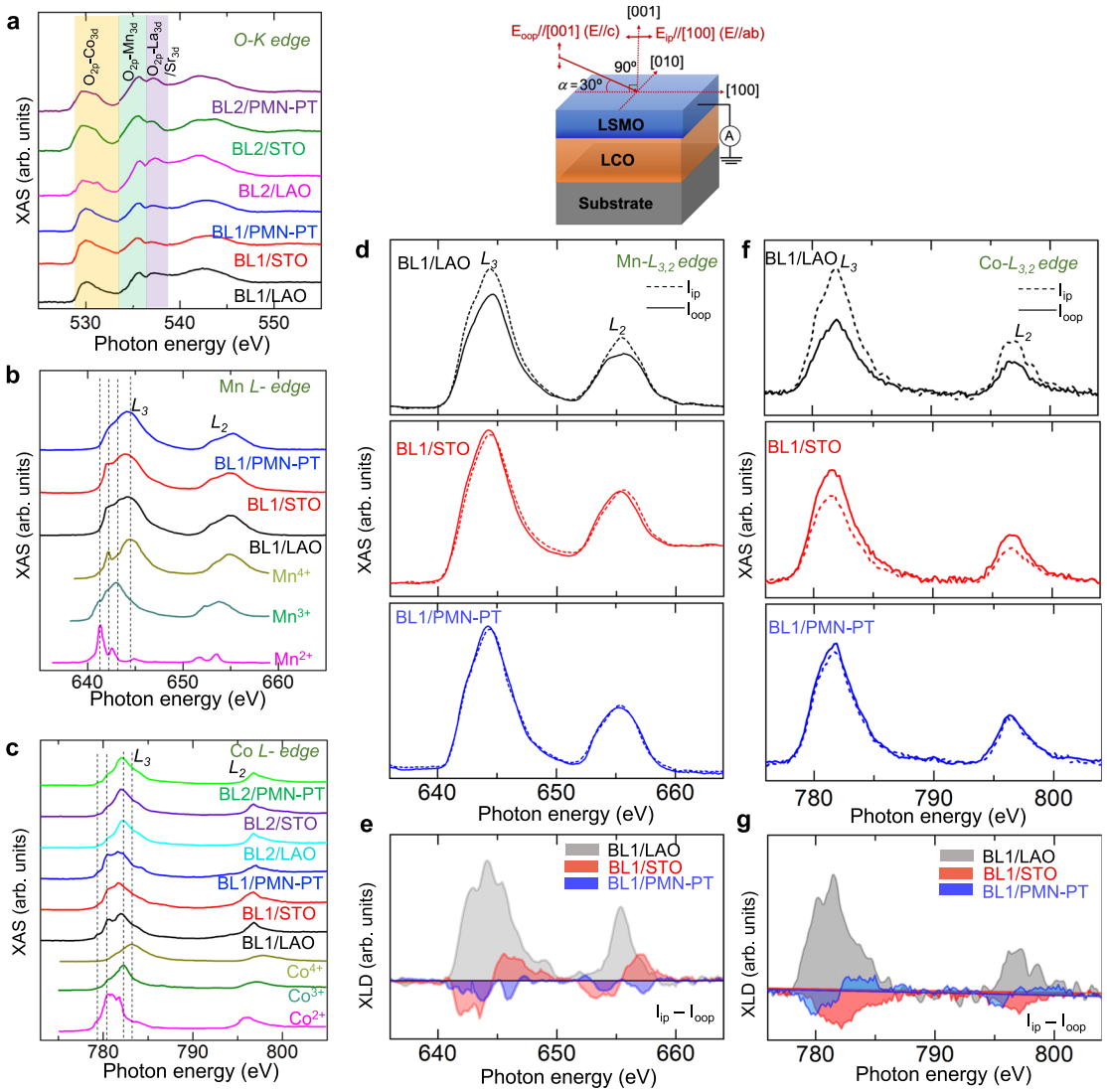

Fig. 3 | Strain mediated electronic structure and orbital polarization in the LSMO/LCO BLs. Elemental specific **a** XAS at O *K*-edge for both sequence bilayers (BL1 and BL2). The colored area in XAS O *K*-edges represents the electronic hybridization between O 2*p* and Co 3 *d* orbitals (transparent yellow); O 2*p* and Mn 3 *d* orbitals (transparent green) and O 2*p* and La/Sr 3 *d* orbitals (transparent purple). **b** XAS measurement done on BL1 with Mn^{2+}, Mn^{3+}, and Mn^{4+} references at the Mn $L_{3,2}$-edges, the peak positions indicate that the BL1 are in mixed $Mn^{4+/3+}$ states. XAS data confirm the valence state of the Mn independent of the strain states for the BLs. The spectra are vertically shifted for clarification. The details of Mn reference spectra are described in Supplementary Note III. **c** XAS at the Co $L_{3,2}$-edge for BL1, BL2 show strong peaks at around 782.06 eV and 780.36 eV in consistent with the Co^{3+} and Co^{2+} ions respectively, which is independent of the strain states. The details of Co reference spectra are described in Supplementary Note III. **d-f** XAS measured from linearly polarized x-ray parallel to the in-plane direction of the sample surface at the Mn $L_{3,2}$-edge (**d**) and Co $L_{3,2}$-edge (**f**) of the BL1 (measurement geometry at the top). **e** The XLD was obtained from the difference for XAS measured with I_{ip} and I_{oop}, i.e. (I_{ip}-I_{oop}) for the BLs. The XLD spectra reveal higher out-of-plane orbital occupancy ($d_{3z^2-r^2}$ d_{zx}, and d_{yz} orbital) for the BL under compressive strain i.e. BL on LAO, while, in-plane orbital occupancy ($d_{x^2-y^2}$ and d_{xy} orbital) for the BL under tensile strain i.e. BL on STO and PMN-PT, indicating a clear anisotropic orbital occupancy induced in Mn 3 *d* e_g orbitals (**e**) and in Co $L_{3,2}$-edge (**g**) by substrate induced strain. All spectra are collected at room temperature.

any experimental errors. This substantiates the fact that compressive strain at the LSMO/LAO interface suppresses octahedral tilt in the LSMO layer of the BL films.

Tuning orbital occupancy: linear dichroism

To probe the impact of structural distortions on the charge reconstruction and orbital occupation in the BLs under strain, we performed element-specific XAS and XLD measurements in total electron yield (TEY) mode (Fig. 3, Supplementary Fig. 17; details in Methods). The features at the O *K*-edge XAS (Fig. 3a) show overlapped peaks within 526–533 eV due to O 2*p*-Co 3 *d* and O 2*p*-Mn 3 *d* hybridized region corresponding to excitations from the O 1*s* state. A clear distinction can be observed in this first feature between BLs, for BL1 (LSMO/LCO), both O 2*p*-Co 3 *d* and O 2*p*-Mn 3 *d* hybridized region are probed, however, for BL2 (LCO/LSMO), only O 2*p*-Co 3 *d* hybridized region is revealed irrespective of strain. Another feature within the 536-538 eV range suggests the O 2*p*-La 3 *d*/Sr 3 *d* hybridized state, while higher energy features are attributed to the O 2*p*-Co 4 *sp*/4 *s* and O 2*p*-Mn 4*sp*/4*s* hybridized regions[33]. Mn $L_{3,2}$-edge XAS (Fig. 3b) shows mixed-valence $Mn^{3+/4+}$ consistent with stoichiometric single layer LSMO films[34] and with more prominence of Mn^{4+} state in BL1(LSMO/LCO) (Supplementary Note I,I,I). Concurrently, XAS of the Co $L_{3,2}$-edge (Fig. 3c) confirms our stoichiometric films with a mixed charge state of $Co^{2+/3+}$ ions where Co^{2+} is more prominent in BL1 (LSMO/LCO) compared to BL2 (LCO/LSMO). Especially, the effective charge reconstruction i.e. charge transfer from Mn to Co, results in high spin Co^{2+} and Mn^{4+} states at the interface of BL1 (LSMO/LCO), which are intricately linked to crystal field splitting energy (Δ_{cf}). This reconstruction

https://doi.org/10.1038/s41467-025-67042-7

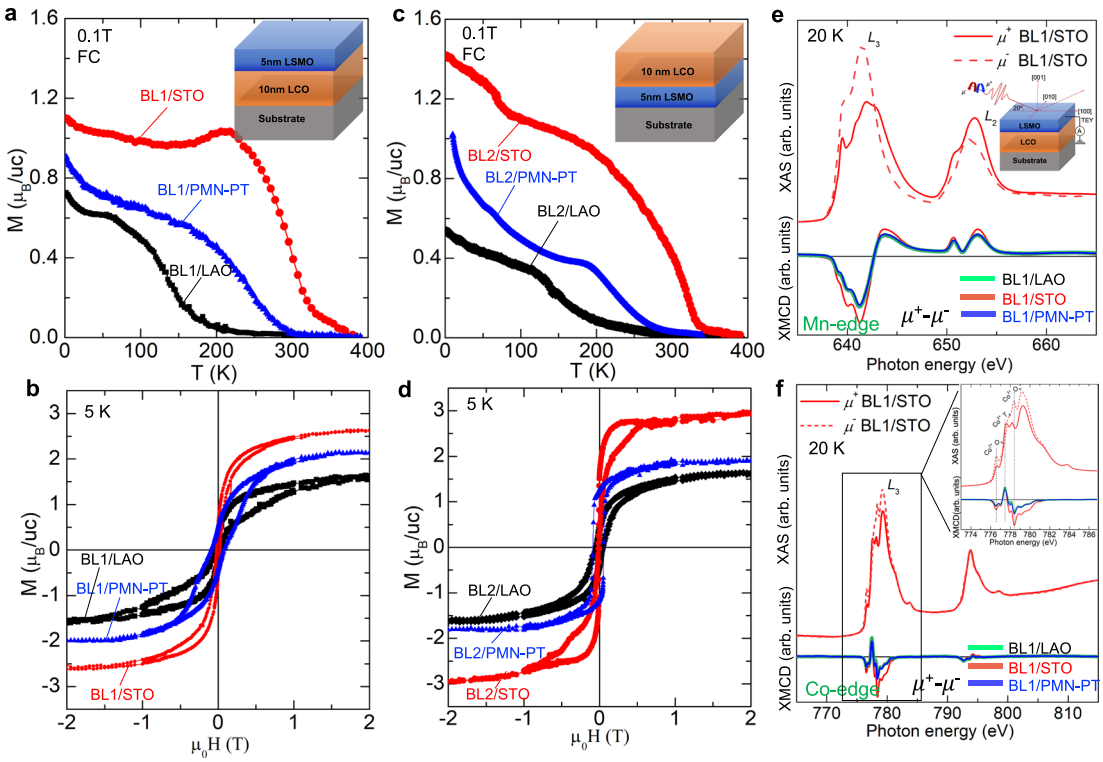

Fig. 4 | Magnetic properties of the BLs under strain. a M-T measured at 0.1 T after field cooled BL1 (BL1 on LAO, STO and PMN-PT). The data shows both LCO and LSMO layer in ferromagnetic nature for BL on STO and PMN-PT (under tensile strain) with an emergence of antiferromagnetic nature in BL on STO, while a suppressed ferromagnetism of LCO is revealed for BL on LAO. **b** M-H loops of the BL1 are recorded at 5 K when a magnetic field is applied along the in-plane direction. BL1 on STO, PMN-PT shows higher saturation magnetization than on BL1 LAO. **c** M-T measured at 0.1 T after field cooled BL2 (BL2 on LAO, STO and PMN-PT). The data indicates the enhanced magnetization for BL on STO, keeping both LCO and LSMO ferromagnetism intact for the BL on STO and PMN-PT, while a spin reorientation around 150 K is seen for BL on LAO substrate. **d** M-H loops of the BL2 recorded at 5 K when a magnetic field is applied along the in-plane direction. BL2 depicts similar behaviour like the BL1 including more enhanced saturation magnetization (with respect to BL1) on STO and PMN-PT. X-ray absorption spectra (XAS) (top panel) at Mn *L*-edges (**e**) and at Co *L*-edge (**f**) were collected at 20 K under 1.2 T field applied at a grazing incidence (20° with respect to the film's surface normal) for the BL1, which is parallel to the incidence beam. The calculated x-ray magnetic circular dichroism (XMCD) spectra (bottom panel of **e**, **f**) for the BL. Non-zero XMCD signal at the Mn *L*-edges and Co *L*-edges is clearly observed for the BLs. Thus, overall magnetization is less under compressive strain and higher in case of tensile strain irrespective of BLs. **f-inset**, Zoomed view at the Co L_3-edge XAS/XMCD of all the BL1s, it is observed that the Co at the interface contains both Co^{2+} & Co^{3+} charge states in the different environments, octahedral (O_h) and tetrahedral (T_d).

is responsive to the variations of Co−O or Mn-O bond length and Co-O-Co or Mn-O-Mn bonding angle changes in determining the essential magnetic properties in BLs.

Furthermore, utilizing XLD, we further characterized the electronic properties of the BLs by probing the unoccupied *d* orbital states of the Mn and Co in the BLs. XLD is calculated by varying the incidence angle (α) of a linearly polarized x-ray beam with respect to the sample's surface plane (Fig. 3d-f and Supplementary Fig. 17; details in Method and Supplementary Note I,I,I). When $\alpha = 90°$ (dashed lines), i.e., the polarization of the x-ray is parallel to the in-plane direction of the sample surface ($I_{ab} = I_{ip}$ (E_{ip}//[100])), the XAS reflects the in-plane orbital occupancy of d_{xy} & $d_{x^2-y^2}$ orbital. When $\alpha = 30°$ (solid lines) i.e. the polarization of the x-ray is perpendicular to the sample surface, and the XAS probes the unoccupied states in both $d_{x^2-y^2}$ (and/or d_{xy}) and $d_{3z^2-r^2}$ (and/or d_{yz} and d_{zx}) orbitals, with $I_c = I_{oop} = [I_{90°} - I_{30°} \cdot \sin^2 30°)/\cos^2 30°]$ (E_{oop}//[001])[35]. To simplify the calculations, the signal of ($I_{ip} - I_{oop}$) can indirectly reflect the orbital asymmetry of the 3 *d* band and is roughly proportional to the exact XLD signals (Fig. 3e, g). Negative to positive XLD values at both the Mn and Co $L_{3,2}$-edges of the BLs for tensile (BL on STO and BL on PMN-PT) to compressively strained (BL on LAO) suggest a highly occupied $d_{x^2-y^2}$ (and/or d_{xy}) orbital to highly occupied $d_{3z^2-r^2}$ (and/or d_{yz} and d_{zx}) orbital, respectively (Fig. 3e, g; Supplementary Fig. 17 and Supplementary Note I,I,I). Here, the orbital reconstruction is attributed to the strong covalent bond formed between the Mn-3*d* & Co-3*d* orbitals through the O-2*p* orbital across the interface and under different strains of the BLs induced by the substrates, elucidated in terms of molecular orbital theory (Supplementary Figs. 22-25 and Supplementary Note I,I,I).

Switching of ferromagnetic order and magnetic ground state

We now delve into a detailed understanding of macroscopic and microscopic insights into magnetic properties under compressive to tensile strain of the BLs (Fig. 4 and details in Methods). Thermal magnetization (M-T) of the BLs reveals finite magnetic moments, transitioning from ferromagnetic to paramagnetic near or above room temperature (Fig. 4a, c). In contrast to the previously reported single-layer 5 nm LSMO ($T_C = 260$ K) and LCO ($T_C = 80$ K)[35,36], the BL on STO shows distinctive transitions: a paramagnetic-to-ferromagnetic shift (attributed to LSMO, $T_C \sim 340$ K), followed by a second transition at 77 K (attributed to LCO). Here, the tensile strain alone proves insufficient for stabilizing LCO's long-range ferromagnetic order of the BL on STO[37]. Moreover, in BL1 (LSMO/LCO) on STO, a decrease of magnetization is observed around 210 K to 82 K, which is assigned to the pinned antiferromagnetic layers at the LSMO/LCO interfaces. In particular, the tensile strain affects the octahedral rotation of the BLs (both on STO and PMN-PT substrates), resulting in an elevated value of T_C (LSMO) in comparison to the measurement recorded in the single-layer LSMO system ($T_C = 260$ K)[35]. The results vividly illustrate the prevailing ferromagnetic nature of LCO and LSMO for both the BL1

(LSMO/LCO) and BL2 (LCO/LSMO) on LAO, STO, and PMN-PT substrates. Specifically, the BLs on the LAO substrate exhibits a marked suppression of ferromagnetic order as compared to those on STO and PMN-PT. This reduction in magnetism can be attributed to strain-induced structural distortions in the LCO layer. Previous studies have shown that ferromagnetic ordering in LCO is highly sensitive to the Co–O–Co bond angle, with significant suppression observed when this angle deviates from 175°[28,38]. Our atomic-resolution AC-STEM analysis (Fig. 2m) reveals a reduction in the Co–O–Co bond angle to ~172°, as determined from the using the equivalent O-O-O_{proj}, directly supporting the observed suppression of ferromagnetism on LAO. Despite this structural distortion, the presence of a finite Co $L_{3,2}$-edges XMCD signal (Fig. 4), confirms that the LCO layer retains a remnant ferromagnetic character, which will be discussed in the following section. This indicates that the compressive strain imposed by the LAO substrate, along with interfacial bond engineering effects at the LCO/LSMO interface, significantly modifies the overall magnetic contributions. In the case of the BLs on PMN-PT substrate, an enhancement in magnetization is observed close to 300 K, attributable to the T_C of LSMO, and a pronounced jump occurs near 87 K due to the T_C of LCO. Compared to STO, PMN-PT exhibits a larger tensile strain, although T_C and magnetization are lower than STO, which can be correlated to the partial relaxation and the presence of edge dislocations in the LSMO layer, as seen from HAADF-STEM (Supplementary Fig. 8). Additionally, a genuine electric-field-dependent response (electric field E = 400 V ≈ 8 kV/cm^2, corresponding to an induced compressive strain of ~ −0.1%) resulting in enhanced magnetization has been observed in the BL2 (LCO/LSMO)/PMN-PT bilayer (Supplementary Fig. 18). The field-dependent magnetization, M (H), for the bilayers, obtained at 5 K (Fig. 4b, d, detailed in Methods), reveals a distinct trend associated with strain effects. The magnetization is higher under tensile strain and lower under compressive strain, highlighting the interplay between ferromagnetic and antiferromagnetic correlations in the LSMO and LCO layers. Specifically, the ferromagnetic correlation weakens as the system transitions from in-plane tensile strain (STO, PMN-PT) to compressive strain (LAO)[39]. This trend is further supported by the observed increase in coercivity and asymmetry from STO to LAO substrates in both BL1 and BL2, which indicates a strengthening of antiferromagnetic correlations under compressive strain.

To gain a proper understanding of the magnetic properties, especially the interfacial magnetization, elemental specific XMCD measurements are performed on the BLs at both the Mn and Co $L_{3,2}$-edge at 20 K, 50 K, and room temperature (Fig. 4e-f and Supplementary Figs. 19-21). In a close inspection of the zoomed view at the Co L_3-edge XAS/XMCD of all the BL1s, it is observed that the Co at the interface contains both Co^{2+} & Co^{3+} charge states in the different environments, octahedral (O_h) and tetrahedral (T_d) (Fig. 4f-inset, Supplementary Fig. 22)[40]. The XAS measured at μ^+/μ^- helicities for BL1/STO and XMCD ($\mu^+ - \mu^-$) of all three BL1s at both the Mn & Co L-edges (Fig. 4e-f). The $Co^{2+}(T_d)$ L_3-edge XMCD signal shows an opposite sign with the Mn L_3-edge XMCD, divulging an antiferromagnetic coupling between the $Co^{2+}(T_d)$ & $Mn^{3+/4+}$ moment at the interface. Whereas the $Co^{2+}(O_h)$ and $Co^{3+}(O_h)$ L_3-edge XMCD signal show the same sign as the Mn L_3-edge XMCD, indicating ferromagnetic alignment between $Mn^{3+/4+}$ and $Co^{2+}(O_h)$ & $Co^{3+}(O_h)$ at the interface although the overall Co L-edge XMCD integral show the same sign as that at the Mn L-edge. We also performed XMCD sum rules to calculate the orbital and spin moment separately as discussed in the Supplementary Note I,I,I and Supplementary Fig. 23. Interestingly, for BL on LAO, the near absence of Co XMCD signal reveals that LCO has drastically suppressed magnetism of the BL on LAO. This antiparallel Mn/Co moment orientation can be further elucidated through molecular orbital considerations (Supplementary Fig. 24-27, Supplementary Note I,I,I). For the BL under compressive strain (BL on LAO), the majority Mn $d_{3z^2\text{-}r^2}$ electron occupies a bonding orbital with the corresponding Co orbital, aligning parallel to the majority t_{2g} spins of Mn in accordance with Hund's rule (Supplementary Fig. 24). Conversely, the minority Co t_{2g} d_{yz} and d_{zx} electrons occupy bonding orbitals alongside the corresponding Mn orbitals, exhibiting an antiparallel alignment with the localized Mn t_{2g} spins, thereby inducing an antiferromagnetic Mn/Co ordering at the interface of the BL (Supplementary Fig. 25). It is noteworthy that both LSMO and LCO under strained conditions exhibit a ferromagnetic state. Analogously, in the case of BL under tensile strain (BL on STO and BL on PMN-PT), an interfacial antiparallel Mn/Co alignment is also established (Supplementary Fig. 25). This unusual interfacial antiferromagnetic Mn/Co ordering in lieu of vivid ferromagnetism of the BLs are further confirmed through Goodenough-Kanamori-Anderson (GKA) rules[39,41] According to the GKA rules, the Mn $d_{3z^2\text{-}r^2}$-(O $2p_{zz}$)-Co d_{yz} and Mn $d_{3z^2\text{-}r^2}$-(O $2p_{zz}$)-Co d_{zx} interactions in the BLs are antiferromagnetic in nature (Supplementary Figs. 26-27) similar to LSMO/$BaTiO_3$[42] heterostructures. Furthermore, the non-zero Mn L-edge XMCD at room temperature (300 K) confirms the ferromagnetic ground state of the LSMO layer in the BLs on STO and PMN-PT (BL under tensile strain). However, there is no such magnetic order observed for the BL on LAO, which is further confirmed by macroscopic magnetization data (Fig. 4 and Supplementary Fig. 20). Here, the detailed measurement of electric field-dependent magnetization at the Mn/Co interface is significantly challenging since the Total Electron Yield (TEY), which relies on drain current measurements, can experience reduced accuracy when an external voltage is applied. On the other hand, the Fluorescence Yield (FY) mode, while offering greater bulk sensitivity with a probing depth of approximately 100 nm, is not suitable for investigating interfacial modifications. Thus, strain-interface engineering plays a key role in manipulating magnetic properties in Co/Mn heterostructures.

Theoretical results

To establish the theoretical foundation of our experimental results, we performed the first-principles calculations on antiferromagnetically coupled ferromagnetic layers of LSMO and LCO oriented along the [001] crystallographic direction (Fig. 5, details in Methods). It is worth mentioning that the FM ordering within the individual LSMO and LCO layers and an antiparallel magnetic moment orientation at the interface are also evident from the experimental observation. We construct a theoretical model of the LSMO–LCO bilayer, comprising alternating layers of LSMO and LCO, each three-unit cells thick—referred to hereafter as the (3/3)-LSMO/LCO bilayer. In this configuration, each layer hosts six magnetic atoms (Mn in LSMO and Co in LCO), leading to a total of twelve magnetic sites per unit cell of the heterostructure. A representative 2 × 2 × 1 supercell of this structure is shown in Fig. 5a. The primary objective of the theoretical model is to explore how strain-induced variations in bond lengths and bond angles influence the magnetic properties of the heterostructure. The layer-resolved analysis of strain modulated magnetic moments in the relaxed LSMO-LCO heterostructures demonstrates strong alignment with experimental data, revealing that tensile strain enhances the magnetic moment of each layer, while compressive strain suppresses it (Supplementary Table 1). The relaxed geometries, which ensure a comparable local environment for La and Sr atoms, reveal a complex interplay between bond lengths, bond angles, and the resulting magnetic moments under varying strain conditions (Supplementary Tables 2–3). In particular, the magnetic moments of Mn and Co atoms exhibit a clear reduction under compressive strain, decreasing from 2.91 μ_B to 2.80 μ_B for Mn, and from −1.91 μ_B to −1.84 μ_B for Co. This reduction correlates with a concomitant contraction in the in-plane metal–oxygen bond lengths. Under tensile strain, the average Mn–O and Co–O bond lengths are 1.92 Å and 1.96 Å, respectively, whereas compressive strain reduces them to 1.85 Å and 1.86 Å. In contrast, the out-of-plane Mn–O and Co–O bond lengths exhibit an elongation under compressive strain, increasing from 1.92 Å to 2.02 Å, and 1.95 Å

https://doi.org/10.1038/s41467-025-67042-7

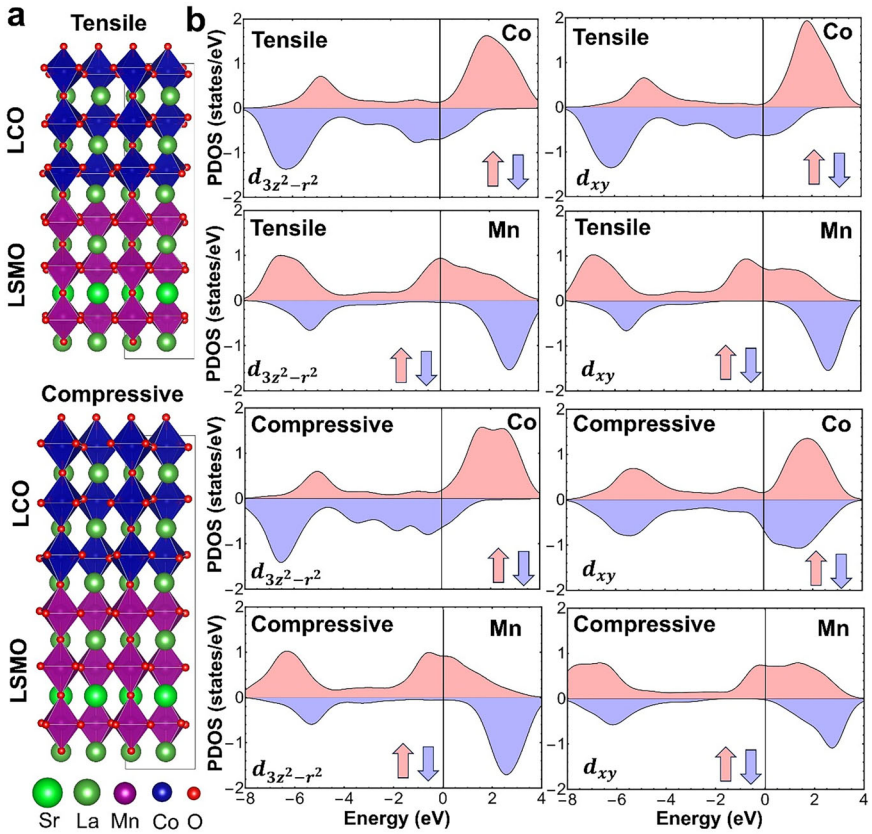

Fig. 5 | Strain induced modulation of in-plane and out-of-plane *d*-orbital contributions of Mn and Co in relaxed 3/3-LSMO/LCO bilayers. a Relaxed geometry of the 3/3-LSMO/LCO bilayer along [001] direction in presence of tensile and compressive strain. In the DFT study the lattice parameters are a = 5.39 Å, b = 5.45 Å, c = 22.94 Å for tensile strain and a = 5.12 Å, b = 5.19 Å, c = 24.63 Å for compressive strain. In comparison to the initial structure, the in-plane lattice parameters are compressed, leading to an elongation of the c-axis. **b** The projected density of states (PDOS) exhibits the in-plane and out-of-plane *d*-orbital contributions of the Mn and Co atoms of the heterostructure, subjected to two distinct strain regimes. Under tensile strain (top panel), the in-plane d-orbitals become more populated, while under compressive strain (bottom panel), the PDOS shows increase in the occupancy of out-of-plane d-orbitals of both Mn and Co atoms. This strain-induced orbital redistribution is visualized by the pink and violet colours, representing the spin-up and spin-down states, respectively. The Fermi level is set at zero energy for reference.

to 2.05 Å, respectively. Additionally, compressive strain induces a notable reduction in the in-plane Mn–O–Mn and Co–O–Co bond angles—from 172° to 161°, and from 158° to 154°, respectively—indicative of enhanced octahedral tilting. The above reduction in bond angles under compressive strain weakens the magnetic exchange interactions, thereby leading to a decrease in the magnetic moments of Mn and Co atoms—a trend that is consistent with experimental observations. To gain deeper insight into the pivotal role of strain-induced O–O–O bond angle modulation in controlling the magnetic properties of the heterostructure, we extend our analysis to two additional configurations: (3/3)-LMO/LCO and (2/2)-LSMO/LCO (Supplementary Figs. 29-30). The (3/3)-LMO/LCO structure is analogous to the (3/3)-LSMO/LCO bilayer, but with the partial Sr occupancy in LSMO omitted—essentially representing the parent compound $LaMnO_3$. Especially, strain in the system described above also leads to a modulation of the in-plane O–O–O bond angle, analogous to the behavior observed in the (3/3)-LMO/LCO superlattice (Supplementary Note IV). This indicates a similar strain-driven tuning of the magnetic moment—as we will explore in the following discussion. Furthermore, in the (2/2)-LSMO/LCO configuration (Supplementary Fig. 30), the LSMO and LCO layers alternate every two-unit cell, reducing the periodic thickness along *c*-axis and offering further insight into the interface-driven effects.

It is noteworthy that for the (3/3) LSMO/LCO heterostructure subjected to in-plane compressive strain, the lattice parameters along the *a*- and *b*-axes were constrained to 5.12 Å and 5.19 Å, respectively, while the out-of-plane lattice constant (*c*) was determined via variable-cell relaxation and found to be 24.63 Å. Under in-plane tensile strain, the in-plane lattice parameters expanded to 5.39 Å and 5.46 Å, accompanied by a reduction in the relaxed out-of-plane lattice constant to 22.94 Å. The (3/3) LMO/LCO bilayer exhibits a similar strain-dependent lattice and magnetic response as the (3/3) LSMO/LCO system (Supplementary Note IV). Under compressive strain, significant reductions in Mn and especially Co magnetic moments correlate with shortened in-plane bond lengths and decreased O–O–O bond angles, highlighting the pronounced strain sensitivity of the LCO layer (Supplementary Note IV, Supplementary Tables 4-6). Also, for the (2/2) LSMO/LCO heterostructure, the optimized *c*-axis lattice constants were calculated to be 15.18 Å and 16.23 Å under tensile and compressive strain, respectively, further confirming the strain-induced anisotropic lattice distortion (Supplementary Tables 7-9).

Furthermore, the (2/2) LSMO/LCO heterostructure successfully reproduces the experimentally observed trend in strain-induced modulation of magnetic moments, as summarized in Supplementary Table 7. This behavior is corroborated by strain-dependent variations in bond lengths and bond angles (Supplementary Tables 8-9). Under compressive strain, the average magnetic moment of Mn decreases from 2.81 μ_B to 2.76 μ_B and that of Co from −1.83 μ_B to −1.63 μ_B consistent with the weakening of magnetic exchange interactions. Correspondingly, under tensile strain, the average in-plane Mn–O and Co–O bond lengths are both 1.94 Å, while the out-of-plane bond lengths are 1.89 Å and 1.95 Å, respectively. Under compressive strain,

the in-plane bond lengths contract to 1.84 Å (Mn–O) and 1.87 Å (Co–O), while the out-of-plane bond lengths expand to 2.05 Å and 2.00 Å, respectively. Consistent with the previous case, the in-plane O–O–O angles decrease from 171° (LSMO) and 161° (LCO) to 166° (LSMO) and 154° (LCO). We note that the OOO_{Proj} angle serves as an effective proxy for the corresponding B–O–B bond angle at the LCO/LSMO interface, showing greater sensitivity to compressive strain and less variation under tensile strain—a trend also supported by experimental observations (Fig. 2).

This strain-driven magnetic moment change can be explained more accurately by the asymmetric projected density of states (PDOS) for spin-up and spin-down electrons, especially the *d*-orbitals of Mn and Co atoms, as depicted for the relaxed bilayers in Fig. 5 and Supplementary Figs. 28–30. The PDOS spectra essentially provide a comprehensive understanding of the strain-induced orbital reconstruction leading to this intricate magnetic behavior. Here, to understand the role of strain on different in-plane and out-of-plane *d*-orbital, we studied the proportion by which the in-plane and out-of-plane occupied *d*-orbitals of the magnetic atoms (say, Mn) change with application of external strain. A detailed discussion on the role of in-plane and out-of-plane *d*-orbital occupancy in the strain-induced variation of magnetic moments is provided in Supplementary Note V, with the corresponding data summarized in Supplementary Tables 10–13. It has been observed for all the cases that the ratio of the magnetic contribution from of the out-of-plane *d*-orbital and the in-plane one increases with compressive strain decreases with the tensile strain in both the layer. These first principles result on the orbital occupancy lend support to our experimental observations on XAS and XLD measurements (Fig. 3). Furthermore, Bader charge analysis (Supplementary Note V) reveals a significant charge imbalance at the interface, indicating substantial charge transfer between the layers. This interfacial charge redistribution plays a key role in modifying the electronic structure of the heterostructure.

In conclusion, our innovative methodology has unveiled an unconventional strategy that utilizes OOO_{proj} angles, replacing the traditional BOB_{proj} angles, to efficiently explore oxygen octahedral tilt in perovskite oxides. Here, we disclose the effects of substrate-induced epitaxial strain on switching the spin state and orbital occupancy between in-plane and out-of-plane orbitals. We reveal previously unreported octahedral tilt that directly correlates with the enhanced magnetism of LCO layers in BL on STO, while strain-mediated OOO_{proj} angle variation depicts the real absence of ferromagnetism of LCO in the BL on LAO substrate. XMCD results and the explanation in the light of molecular orbital theory confirm the antiferromagnetic involvement of Mn/Co interfaces. First principles theoretical calculations further clearly demonstrate the scenario of strain-induced Co/Mn individual magnetic moment contribution and interfacial antiferromagnetism, in-plane and out-of-plane orbital occupation, and detailed bond angle geometry specifically in terms of OOO_{proj}. Thus, the interplay of octahedral tilt and charge-spin-orbital reconstruction in oxide heterostructures offers a promising strategy to interface-engineer physical properties, such as voltage-controlled strain or orbital filling. This approach holds significant promise for the development of efficient low energy spintronics, including magnetic tunnel junction, magnetic field sensing, and devices for magnetic storage applications.

Methods

Sample preparation

The [$LaCoO_3$ (LCO)/$La_{0.7}Sr_{0.3}MnO_3$ (LSMO)] BLs were synthesized on single-crystalline LAO (001), STO (001), PMN-PT (001) substrates via reflection high energy electron diffraction (RHEED)-assisted pulsed laser deposition (KrF laser, λ = 248 nm). Here BLs are designed in two reverse sequences where capped LSMO (top) on LCO thin film is denoted as BL1 (LSMO/LCO), while capped LCO (top) on LSMO thin film is as BL2 (LCO/LSMO). Firstly, 5 nm LSMO was grown on all the substrates at substrate temperature (T_S) of 700 °C in 100 mTorr of oxygen pressure (P_{O2}). On this LSMO bottom layer, a 10 nm LCO top layer was grown with (P_{O2}) = 300 mTorr at the same T_S. A similar protocol was followed to grow the bilayer configuration consisting of a bottom layer of 10 nm LCO and top layer of 5 nm LSMO on those substrates at the same T_S with P_{O2} = 300 and 100 mTorr respectively. For all materials, the laser fluence was 0.6 J/cm^2 with a repetition rate of 4 Hz. After deposition, the bilayers were annealed for 30 min in 50 Torr of oxygen pressure to ensure the correct oxygen stoichiometry and then cooled down to room temperature at that oxygen pressure. RHEED intensity before and after the growth of each layer is shown in Supplementary Fig. 1.

Structural and surface morphology characterization

X-ray diffraction (XRD), and reciprocal space mapping (RSM) measurements were carried out using a Bruker D8 discover diffractometer with Cu-*Kα* radiation (λ = 1.54056 Å) (Supplementary Figs. 4-5). The morphologies and roughness of substrates as well as samples were characterized with an Asylum Research Oxford 3D origin plus AFM in the tapping mode.

Magnetic measurements

Temperature and field dependence microscopic magnetic measurements are performed by using a Quantum Design VSM SQUID (superconducting quantum interference device). The temperature-dependent (*M-T*) in-plane ($\mu_0 H$//100) magnetic measurements were recorded at 0.1 T after the field cooling (FC). The magnetic hysteresis curves (M-H) are measured along in-plane ($\mu_O H$//100) direction at 10 K after the field cooling samples (FC) at 0.1 T. The magnetization of the films was acquired by subtracting the diamagnetic signals from the substrates and the plastic tube. The magnetization is expressed in Bohr magnetons per total number of pseudo-cubic unit cells.

STEM measurements

The cross-sectional samples for STEM were prepared using an FEI Scios FIB-SEM dual beam system using Ga^+ ions. The single-crystal foil was thinned along the particular zone axis required (i.e,. STO, LAO [110]), to minimize the tilting required in the STEM as too much tilting (roughly >5°) will cause thickness-related artifacts in the ABF mode. The final cleaning was done using an Ar ion beam in a Gatan PIPS II system. The STEM imaging was performed in an FEI Titan Themis equipped with a CEOS probe C_s corrector, operated at 300 kV. A 70 μm C2 aperture and a camera length of 160 mm was used, such that the ABF image could be acquired using the DF2 detector, while simultaneously acquiring the HAADF image using the high-angle detector. The sample was tilted to the zone axis and allowed to stabilize for at least 1 hour, before acquiring the data. Further, the scan dimension was reduced to allow a longer dwell time (8 μs) per pixel, to improve the signal-to-noise ratio, while minimizing drift. The energy dispersive X-ray spectroscopy (EDS) mapping was done using the Velox software, incorporating a beam current of ~150 pA. The strain concentration in the films were extracted from the HAADF micrographs using the Peak pair analysis (PPA) Digital Micrograph plug-in from HREM Research Inc[43].

Octahedral tiling measurement approach

The coordinates of the A, B and O sites in the ABF micrographs were extracted from the Fourier-filtered ABF micrograph by fitting Gaussians to the peak positions using the Atomap package. The B and O coordinates were then used to measure the in-plane projected B-O-B, O-B-O and O-O-O angles between the multiple octahedra, calculated using a custom script written in Python. All the angles are measured between two consecutive oxygen-sharing octahedra along a row (i.e., the BO plane), taking two octahedra at a time (Code details in Supplementary Note II). To validate the script, ABF images of STO and

LSMO were simulated using Dr. Probe software (Supplementary Fig. 4a and 4f). The simulated images were subject to the Atomap script to extract the coordinates of the B and O sites. The coordinates were then used in the custom script to find the B-O-B, O-B-O and O-O-O angles which were mapped to the respective coordinates and plotted as contours and row-averaged scatter plots (with the standard deviation) for STO and LSMO (Supplementary Fig. 4c, d, e and 4h, i, j). Since we can assume (to a first approximation) that the B-O-B, O-B-O and O-O-O angles are all equal to 180° in the STO, we confirm that the Gaussian fitting through the Atomap script, and the custom angle calculator script succeeds sufficiently. However, when applied to an experimental ABF image of STO, it is observed that only the O-O-O angle is robust and gives the correct value as tabulated in Supplementary Fig. 5. The errors in the B-O-B and O-B-O angles might be the result of experimental error of B site positions or some distortions related to the B sites in the micrograph and will require further investigation (Supplementary Note II). But since the B-O-B and O-O-O angles can be assumed to be equal in LSMO (Along the projection considered, and to a first approximation, schematic in Supplementary Fig. 4g), either can be used to quantify the octahedral tilting. Thus, the O-O-O angle is used throughout the current article. Finally, the tilt mapping procedure has been applied to an experimental LSMO/STO interface micrograph. The coplanarity of the O sites in the STO layer and the non-coplanarity of the O sites in the LSMO layers are observed (Supplementary Fig. 6b-c). A checkerboard pattern is observed in the B-O-B angle contour map (Supplementary Fig. 6d), similar to the octahedral tilt pattern in LSMO, but the absolute tilt angle is deemed inaccurate as the substrate B-O-B angle comes out to be 160°. However, the O-O-O angle from the substrate is closer to 180°, and a clear deviation in the octahedral tilt (close to 10°) is observed when going from the substrate to the film (Supplementary Fig. 6f). The O-O-O angles are used throughout the article and more work is required for the complete understanding of the robustness.

XAS, XMCD and XLD measurements

Element-sensitive XAS and XMCD measurements were performed at P04 beamline, PETRA III, DESY, Germany (and ALBA synchrotron, Barcelona, Spain) at the Mn and Co $L_{3,2}$-edges and O *K*-edge in surface-sensitive total electron yield (TEY) modes at 50 and 300 K at normal incidence under 0.6 T magnetic field (and at 20 K at grazing incidence {20° with respect to the film's surface normal} under 1.2 T magnetic field). The process was carried out under a background vacuum of 8×10^{-7} Torr. The normalization of spectra was performed so that the L_3 pre-edge spectral region was set to zero, in addition to the post L_2 edge region set to one. Circularly polarized x-rays with ~100% polarization were used in normal incidence with respect to the sample surface and parallel to the applied magnetic field. The XMCD was obtained by taking the difference of the XAS spectra of right circularly polarized light (μ^+) and left circularly polarized light (μ^-), i.e., $\mu^+ - \mu^-$, by flipping the magnetic field of ±0.6 T at a fixed X-ray helicity. The intensity and the detailed line shape of the XAS spectra reveal information about different valence states, while those of the XMCD spectra indicate the corresponding magnetic ground states. XLD measurement was performed at BL01 beamline of Indus-2 synchrotron radiation source at RRCAT, Indore using linearly polarized X-rays with polarization vector (E) parallel to the in-plane or out-of-plane direction of the sample plane, respectively in the TEY mode at 300 K.

Theoretical calculations

The first-principles calculations for LSMO-LCO heterostructure are performed under the spin-polarized density functional theory (DFT) framework as implemented in the quantum espresso code[44,45]. We have employed the Perdew-Burke-Ernzerhof (PBE) form for the exchange-correlation functional[46] for all the calculations. Furthermore, the kinetic energy cut-off is set as 75 Ry in our study using the ultrasoft pseudopotentials[47] to describe the core electrons. The Brillouin zone was sampled using a uniform $4 \times 4 \times 3$ k-mesh for the self-consistent field (SCF) calculations. The correlation effects for the Mn and Co sites were evaluated using the DFT + U method with Hubbard U parameters of 2 eV and 2.7 eV, respectively. Specifically, we first performed a full structural optimization (vc-relax), allowing both atomic positions and unit cell parameters to relax to their equilibrium values without any constrain. This step ensures minimization of the total energy and residual stress, yielding a stable reference structure. To explore strain-induced (tensile or compressive) modifications, we then altered the in-plane lattice vectors accordingly and subsequently relaxed only the out-of-plane (c-axis) lattice parameter while keeping the in-plane vectors fixed, allowing the system to reach its new minimum-energy configuration under biaxial strain. Experimentally, both LSMO and LCO layers are observed to maintain FM ordering under varying strain conditions. However, at the interface, their magnetic moments align antiparallel to each other. This experimentally observed magnetic configuration was used as a physically realistic initial guess for the magnetic moment alignment in our self-consistent calculations. In this study, we focus on heterostructures composed of alternating layers of LSMO and LCO, specifically those with three-unit cells of each material —referred to as the (3/3)-LSMO/LCO bilayer configuration. Therefore, each layer contains six magnetic atoms (Mn in LSMO and Co in LCO), resulting in a total of 12 magnetic atoms per full bilayer unit cell. For reference, a $2 \times 2 \times 1$ supercell based on this heterostructure model is shown in Fig. 5(a). We emphasize that the robustness of the strain-induced magnetic properties was further validated using an alternative heterostructure, in which LSMO and LCO layers alternate with a thickness of two unit cells—referred to as the (2/2)-LSMO/LCO bilayer—comprising eight magnetic atoms per unit cell. A detailed discussion of this configuration is provided in the Supplementary Information. Moreover, we demonstrate that the modulation of the magnetic moment due to strain remains robust even when the partial Sr occupancy in LSMO is neglected, as evidenced in the (3/3)-LMO/LCO bilayer system (Supplementary Note IV). To eliminate surface effects and emphasize interfacial contributions, periodic boundary conditions were applied along all three crystallographic directions. In the case of compressive strain, the lattice parameters along the a, b, and c directions of the (3/3)-LSMO/LCO bilayer were 5.12 Å, 5.19 Å, and c = 24.63 Å, respectively while, under in-plane tensile strain, the corresponding lattice constants were 5.39 Å, 5.45 Å, and 22.94 Å. For the (2/2)-LSMO/LCO bilayer, the lattice constants along the c-axis under tensile and compressive strain were found to be 15.19 Å and 16.24 Å, respectively. Finally, non-self-consistent field (NSCF) calculations were performed to evaluate the projected density of states (PDOS) of the d orbitals of the Mn and Co atoms in the heterostructure.

Data availability

All the data needed to reach to the conclusions in the paper are present in the paper or the Supplementary section. Relevant data are available upon request from the corresponding authors. Source data are provided with this paper.

References

1. Hwang, H. et al. Emergent phenomena at oxide interfaces. *Nat. Mater.* **11**, 103–113 (2012).
2. Tokura, Y. & Nagaosa, N. Orbital physics in transition-metal oxides. *Science* **288**, 462–468 (2000).
3. Bristowe, N. et al. Ferromagnetism induced by entangled charge and orbital orderings in ferroelectric titanate perovskites. *Nat. Commun.* **6**, 6677 (2015).
4. Pesquera, D. et al. Beyond Substrates: Strain Engineering of Ferroelectric Membranes. *Adv. Mater.* **32**, 2003780 (2020).
5. Torres, P. et al. Giant electrophononic response in $PbTiO_3$ by strain engineering. *Phys. Rev. Lett.* **123**, 185901 (2019).

6. Bang, J. et al. Interface engineering for substantial performance enhancement in epitaxial all-perovskite oxide capacitors. *NPG Asia Mater.* **15**, 4 (2023).
7. Liu, C. et al. Probing the Néel-Type Antiferromagnetic Order and Coherent Magnon–Exciton Coupling in Van Der Waals VPS3. *Adv. Mater.* **35**, 2300247 (2023).
8. Sun, Y. et al. Defect engineering in perovskite oxide thin films. *Chem. Commun.* **57**, 8402–8420 (2021).
9. Menéndez, C. et al. Oxygen-vacancy induced magnetic phase transitions in multiferroic thin films. *npj Comput Mater.* **6**, 76 (2020).
10. Zhang, J. et al. Symmetry mismatch-driven perpendicular magnetic anisotropy for perovskite/brownmillerite heterostructures. *Nat. Commun.* **9**, 1923 (2018).
11. Ding, X. et al. Crystal Symmetry Engineering in Epitaxial Perovskite Superlattices. *Adv. Funct. Mater.* **31**, 2106466 (2021).
12. Jeong, S. G. et al. Propagation Control of Octahedral Tilt in $SrRuO_3$ via Artificial Heterostructuring. *Adv. Sci.* **7**, 2001643 (2020).
13. Beanland, R. Structure of planar defects in tilted perovskites. *Acta Crystallogr.* **A67**, 191–199 (2011).
14. Liao, Z. et al. Long-range domain structure and symmetry engineering by interfacial oxygen octahedral coupling at heterostructure interface. *Adv. Funct. Mater.* **26**, 6627–6634 (2016).
15. Garcia-Castro, A. C. et al. Octahedral distortion and electronic properties of the antiperovskite oxide Ba3SiO: First principles study. *J. Phys. Chem. Solids* **136**, 109126 (2020).
16. Junwen, Y. et al. Tuning Octahedral Tilting by Doping to Prevent Detrimental Phase Transition and Extend Carrier Lifetime in Organometallic Perovskites. *J. Am. Chem. Soc.* **145**, 5393–5399 (2023).
17. Zhao, H. J. et al. Magnetoelectric effects via pentalinear interactions. *Phys. Rev. B* **92**, 235133 (2015).
18. Yang, Y. et al. Prediction of a Novel Magnetoelectric Switching Mechanism in Multiferroics. *Phys. Rev. Lett.* **112**, 057202 (2014).
19. Bechtel, J. S. et al. Octahedral tilting instabilities in inorganic halide perovskites. *Phys. Rev. Mater.* **2**, 025401 (2018).
20. Chowdhury, S. et al. Strain dependent spin-blockade effect realization in the charge-disproportionated $SrCoO_{2.5}$ thin films. *Appl. Phys. Lett.* **119**, 021901 (2021).
21. Freeland, J. W. et al. Orbital control in strained ultra-thin $LaNiO_3$/$LaAlO_3$ superlattices. *EPL* **96**, 57004 (2011).
22. Wakabayashi, Y. K. et al. Ferromagnetism above 1000 K in a highly cation-ordered double-perovskite insulator Sr_3OsO_6. *Nat. Commun.* **10**, 535 (2019).
23. Rondinelli, J. M. et al. Structure and Properties of Functional Oxide Thin Films: Insights From Electronic-Structure Calculations. *Adv. Mater.* **23**, 3363 (2011).
24. Van Aken, B. B. et al. The origin of ferroelectricity in magnetoelectric $YMnO_3$. *Nat. Mater.* **3**, 164 (2004).
25. Cohen, R. E. Origin of ferroelectricity in perovskite oxides. *Nature* **358**, 136 (1992).
26. Fujioka, J. et al. Strain-sensitive spin-state ordering in thin films of perovskite $LaCoO_3$. *Phys. Rev. B* **92**, 195115 (2015).
27. Sterbinsky, G. E. et al. Ferromagnetism and Charge Order from a Frozen Electron Configuration in Strained Epitaxial $LaCoO_3$. *Phys. Rev. Lett.* **120**, 197201 (2018).
28. Guo, E.-J. et al. Switchable orbital polarization and magnetization in strained $LaCoO_3$ films. *Phys. Rev. Mater.* **3**, 014407 (2019).
29. Li, X. et al. Impact of interfacial coupling of oxygen octahedra on ferromagnetic order in $La_{0.7}Sr_{0.3}MnO_3$/$SrTiO_3$ heterostructures. *Sci. Rep.* **7**, 40068 (2017).
30. Lepetit, M. et al. Interface effects in perovskite thin films. *Phys. Rev. Lett.* **108**, 087202 (2012).
31. Lee, J. S. et al. Hidden magnetic configuration in epitaxial $La_{1-x}Sr_xMnO_3$ films. *Phys. Rev. Lett.* **105**, 257204 (2010).
32. May, S. J. et al. Enhanced ordering temperatures in antiferromagnetic manganite superlattices. *Nat. Mater.* **8**, 892–897 (2009).
33. Chowdhury, S. et al. Electronic Phase Switching in the Negative Charge Transfer Energy $SrCoO_x$ Thin Films with the Mottronic Relevancies. *ACS Appl. Electron. Mater.* **3**, 3060–3071 (2021).
34. Trappen, R. et al. Electrostatic potential and valence modulation in $La_{0.7}Sr_{0.3}MnO_3$ thin films. *Sci. Rep.* **8**, 14313 (2018).
35. Tebano, A. et al. Evidence of orbital reconstruction at interfaces in ultrathin $La_{0.67}Sr_{0.33}MnO_3$ films. *Phys. Rev. Lett.* **100**, 137401 (2008).
36. Shin, Dongwon et al, Tunable Ferromagnetism in $LaCoO_3$ Epitaxial Thin Films. Adv. Mater. Interfaces 2200433 (2022)
37. Rondinelli, J. M. & Spaldin, N. A. Structural effects on the spin-state transition in epitaxially strained $LaCoO_3$ films. *Phys. Rev. B* **79**, 054409 (2009).
38. Joshi, T. et al. Geometric influence on the net magnetic moment in $LaCoO_3$ thin films. *J. Mater. Res.* **38**, 2274–2286 (2023).
39. P. W. Anderson, Phys. Rev. 79, 350 (1950).
40. Galakhov, V. R. X-Ray Spectroscopy of Cobaltites. *Phys. Met. Metallogr.* **122**, 83–114 (2021).
41. J. B. Goodenough, Phys. Rev. 100, 564 (1955).
42. Wang, H. et al. Atomic-Scale Control of Magnetism at the Titanite-Manganite Interfaces. *Nano Lett.* **19**, 3057–3065 (2019).
43. Galindo, P. L. et al. The Peak Pairs algorithm for strain mapping from HRTEM images. *Ultramicroscopy* **107**, 1186–1193 (2007).
44. Giannozzi, P. et al. Advanced capabilities for materials modelling with Quantum ESPRESSO. *J. Phys.: Condens. Matter* **29**, 465901 (2017).
45. Giannozzi, P. et al. QUANTUM ESPRESSO: a modular and open-source software project for quantum simulations of materials. *J. Phys.: Condens. Matter* **21**, 395502 (2009).
46. Perdew, J. P. Generalized Gradient Approximation Made Simple. *Phys. Rev. Lett.* **77**, 3865 (1996).
47. Vanderbilt, D. Soft self-consistent pseudopotentials in a generalized eigenvalue formalism. *Phys. Rev. B* **41**, 7892–7895 (1990).

Acknowledgements

S.D. acknowledges Science and Engineering Research Board (EEQ/2023/000089), Infosys Young Investigator Award, and S.D. and A.N. thanks Indian Institute of Science start up grant for financial support. J.K.D. and A.B. would like to acknowledge IoE-IISc Postdoctoral Fellowship. J.K.D., A.A., A.K., M.G., R.J.C. and S.D. acknowledges the UGC-DAE CSR and RRCAT Indore synchrotron facilities in particularly R. Sah, A. Wadikar and the Accelerator Physics and Synchrotrons Utilization Division of RRCAT. S.D. acknowledges the Collaborative Research Scheme (CRS) of UGC-Indore (CRS/2022-23/104). S.C., F.A., M.H., and S.D. acknowledge DESY (Hamburg, Germany), a member of the Helmholtz Association HGF, for the provision of experimental facilities. Parts of this research were carried out at PETRA III, beamline P04. S.D. acknowledges the DST-DESY partnership. K.J., N.R. and S.D. acknowledges the Advanced Facility for Microscopy and Microanalysis (AFMM) for access to the FIB and STEM.

Author contributions

S.D. designed the experiments. S.D. and J.K.D. grew the samples and performed the structural and magnetic property measurements. K.J. and S.D. performed the STEM. A.A., A.K., M.H., F.A., M.V. and S.C. performed XAS-XMCD. A.B. and A.N. performed the theoretical calculations. J.K.D., S.D., K.J., S.C., A.B., N.R. T.V. analyzed the data and co-wrote the manuscript. B.R., S.B.K., M.G., R.J.C. contributed to the discussions and edit the manuscript. S.D. supervised the research.

Competing interests

The authors declare no competing interests.

Additional information

Supplementary information The online version contains supplementary material available at https://doi.org/10.1038/s41467-025-67042-7.

Correspondence and requests for materials should be addressed to Thirumalai Venkatesan or Sujit Das.

Peer review information *Nature Communications* thanks the anonymous, reviewer(s) for their contribution to the peer review of this work. A peer review file is available.

[1]Materials Research Centre, Indian Institute of Science, Bangalore 560012, India. [2]Solid State and Structural Chemistry Unit, Indian Institute of Science, Bangalore 560012, India. [3]Deutsches Elektronen-Synchrotron DESY, Notkestrasse 85, 22607 Hamburg, Germany. [4]ALBA Synchrotron Light Source, E-08290 Cerdanyola del Vallès, Barcelona, Spain. [5]UGC-DAE Consortium for Scientific Research, University Campus, Khandwa Road, Indore 452001, India. [6]Institute of Sciences, Sage University, Indore 452020 (M.P), India. [7]Department of Physics, Faculty of Science, The Hashemite University, P. O. Box 330127, Zarqa 13133, Jordan. [8]Central Research Laboratory, Bharat Electronics, Bangalore 560013, India. [9]Center for Quantum Research and Technology, University of Oklahoma, Norman, OK 73019, USA. [10]Present address: Deutsches Elektronen-Synchrotron DESY, Notkestrasse 85, 22607 Hamburg, Germany. [11]These authors contributed equally: Jayjit Kumar Dey, Koushik Jagadish, Arka Bandyopadhyay, Sourav Chowdhury. ✉e-mail: venky@ou.edu; sujitdas@iisc.ac.in